Bulletin of the Seismological Society of America, Vol. 103, No. 2B, pp. 1348–1359, May 2013, doi: 10.1785/0120120155

Envelope Inversion Analysis for High-Frequency Seismic Energy Radiation from the 2011 M_w 9.0 Off the Pacific Coast of Tohoku Earthquake

by Hisashi Nakahara

Abstract I study *S*-wave energy radiation in higher frequencies of 1–8 Hz from the 2011 M_w 9.0 Off the Pacific Coast of Tohoku, Japan, earthquake (hereafter called the Tohoku-Oki earthquake) based on a seismogram envelope inversion method. I first evaluate two medium parameters of scattering attenuation and intrinsic absorption for *S* waves using spatial and temporal distributions of seismic energy from aftershock records, which are necessary for calculating Green's functions. Next, applying the envelope inversion method to 27 near-field strong-motion records from the mainshock, I estimate the *S*-wave energy radiation from 40 subfaults on the fault of 500 km × 250 km. Each subfault is allowed to rupture for eight consecutive source time windows. Rupture velocity and the duration of energy radiation for each time window are determined by a grid search to be 2.5 km/s and 8.0 s, respectively. Energy radiated from the entire fault is 5.8×10^{16} J for 1–2 Hz, 4.5×10^{16} J for 2–4 Hz, 1.5×10^{16} J for 4–8 Hz, and totaling 1.2×10^{17} J in the 1–8 Hz range. Strong energy emanated twice from greater depths of the off-Miyagi region, corresponding to two peaks seen at the northern stations. And energy radiation at greater depths off the Fukushima–Ibaraki border is compatible with a single peak found at the southern stations. Strong high-frequency radiations at greater depths strikingly contrast with large slips at shallower depths estimated in lower frequencies. This frequency-dependent rupture may accord with structural changes along the dip direction.

Online material: Snapshots of high-frequency energy radiation from the fault plane and results of estimating scattering parameters by the multiple lapse time window analysis in 1–2 and 2–4 Hz.

Introduction

The 2011 Tohoku-Oki earthquake took place at 14:46 on 11 March 2011 (in Japan Standard Time; UTC + 9 h) at a depth of about 24 km on the plate boundary between the subducting Pacific plate and the overlying landward plate in northeastern Japan (Fig. 1). Strong ground motion was felt over Eastern Japan with the maximum intensity of 7 in the Japan Meteorological Agency scale, corresponding to 10 or more in the modified Mercalli scale. Destructive tsunamis struck cities and towns in the Pacific coast. Casualties of 16,278 have been reported, as well as 2994 missing, as of March 2012 (Fire and Disaster Management Agency, 2012).

Earlier reports on many aspects of this earthquake have been published in a special volume of *Earth, Planets and Space* (Yomogida and Kanamori, 2011) and a special section in *Geophysical Research Letters* (AGU, 2012). Concerning the earthquake source process, one of the peculiar characteristics is a striking contrast between regions of low-frequency wave radiation at shallower depths and those of high-frequency radiation at greater depths (e.g., Ide *et al.*, 2011; Koper *et al.*, 2011; Simons *et al.*, 2011; Kiser and Ishii, 2012). In lower frequencies, teleseismic records, near-field seismograms, geodetic data, and tsunami records were inverted for slip on the fault. In higher frequencies, wave radiation areas were estimated mainly using backprojection of teleseismic and near-field records. A few studies such as Kurahashi and Irikura (2011) estimated strong-motion generation areas on the fault by forward modeling of near-field strong-motion data based on an empirical Green's function method.

In the 1990s, envelope inversion methods were developed (e.g., Gusev and Pavlov, 1991; Zeng *et al.*, 1993; Kakehi and Irikura, 1996) and made it possible to estimate high-frequency seismic wave radiation from faults in higher frequencies than about 1 Hz. The methods correspond to waveform inversion methods in lower frequencies. The

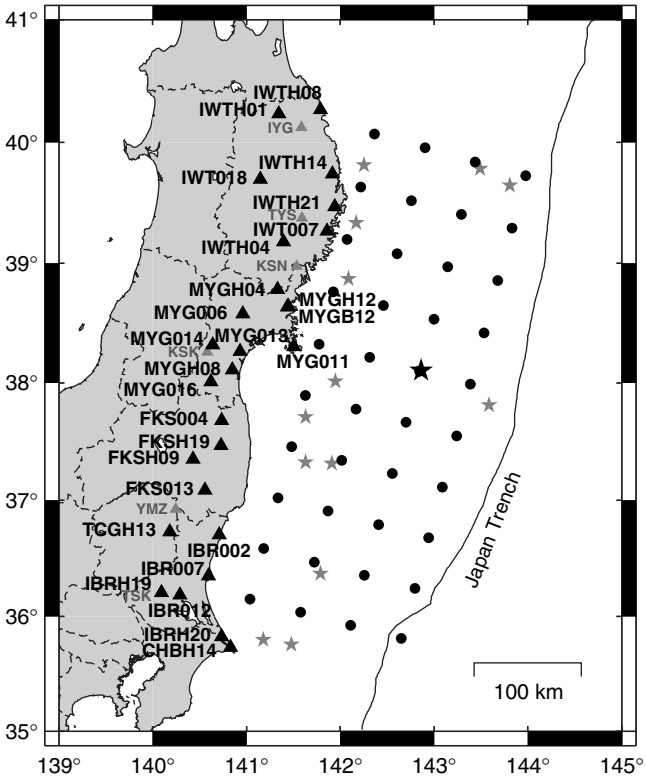

Figure 1 Station distribution and an assumed fault geometry. Solid triangles are 27 stations used for the envelope inversion analysis. A solid star is the epicenter of the Tohoku-Oki earthquake. A fault plane of this earthquake has a length of 500 km, a width of 200 km, strike of 195° and dip of 13°. Solid circles are the center of subfaults, each of which is a 50 km × 50 km square. Gray triangles and gray stars are stations and aftershocks used for estimating parameters of the medium, respectively.

results obtained by the envelope inversions have important implications for studying dynamics of frequency-dependent earthquake ruptures and predicting strong ground motion in broader frequency bands. A summary of the studies is found in Nakahara (2008). In this study, applying an envelope inversion method of Nakahara *et al.* (1998) to near-field strong motion records, I estimate spatial distribution of high-frequency seismic energy radiation from the mainshock fault. And I confirm that high-frequency waves were radiated indeed at greater depths of the fault.

High-Frequency Seismogram Envelope Inversion Analysis

Method

I use the envelope inversion method of Nakahara *et al.* (1998), a schematic illustration of which is shown in Figure 2. I assume an infinite homogeneous medium in which isotropic *S*-wave scatterers are distributed uniformly and randomly. Only scattering from *S* wave to *S* wave is assumed, neglecting conversion scatterings among *P* waves, *S* waves, and surface waves. This assumption is discussed later in the

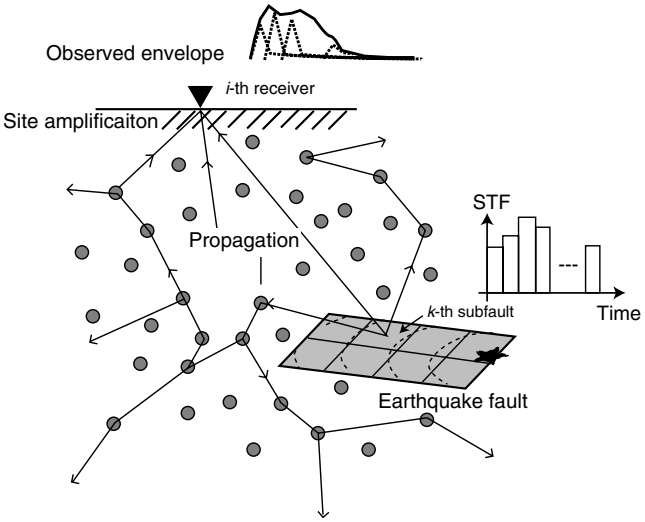

Figure 2 Schematic illustration of the envelope inversion method. Seismic energy radiated from a point shear dislocation source located at the center of the *k*th subfault is multiply scattered by randomly distributed isotropic scatterers (gray circles), attenuated by intrinsic absorption, amplified beneath the *i*th station (solid triangle), and reaches a station at the *j*th time. Each subfault is allowed to radiate seismic energy for eight time windows.

Discussion section. Two parameters of scattering coefficient g_0 and intrinsic absorption coefficient η for *S* waves characterize the medium and control the shape of envelope Green's functions. A fault plane is divided into several subfaults, each of which is broken by the rupture front propagating with a constant velocity. At the *k*th subfault, a point shear-dislocation source radiates seismic wave energy of W_k following the boxcar time function $B(t)$ after the rupture front passes the center of the subfault. Here, multiple time windows are set to allow for multiple ruptures at each subfault and fluctuations in rupture velocity. So the rupture velocity may be called a velocity to trigger the first time window. Radiated seismic energy propagates through the medium and is affected by multiple scattering and intrinsic absorption, and reaches the *i*th station, of which a site amplification factor is S_i. By assuming that energy radiated from all subfaults is additive, the synthesized envelope at the *i*th station and the *j*th time C_{ij} can be written as

$$C_{ij} = S_i^2 \sum_k W_k F_{ijk}.$$

The factor S_i^2 explicitly stands for a site amplification factor for envelopes proportional to squared amplitudes. Function F_{ijk} is a convolution of the envelope Green's function with the boxcar source time function $B(t)$. The envelope Green's function is theoretically calculated based on the radiative transfer theory (Sato *et al.*, 1997) with two medium parameters of g_0 and η, which are estimated by the multiple lapse time window analysis of aftershocks. The details are described in the Appendix. Because this envelope Green's function is derived for a homogeneous background medium,

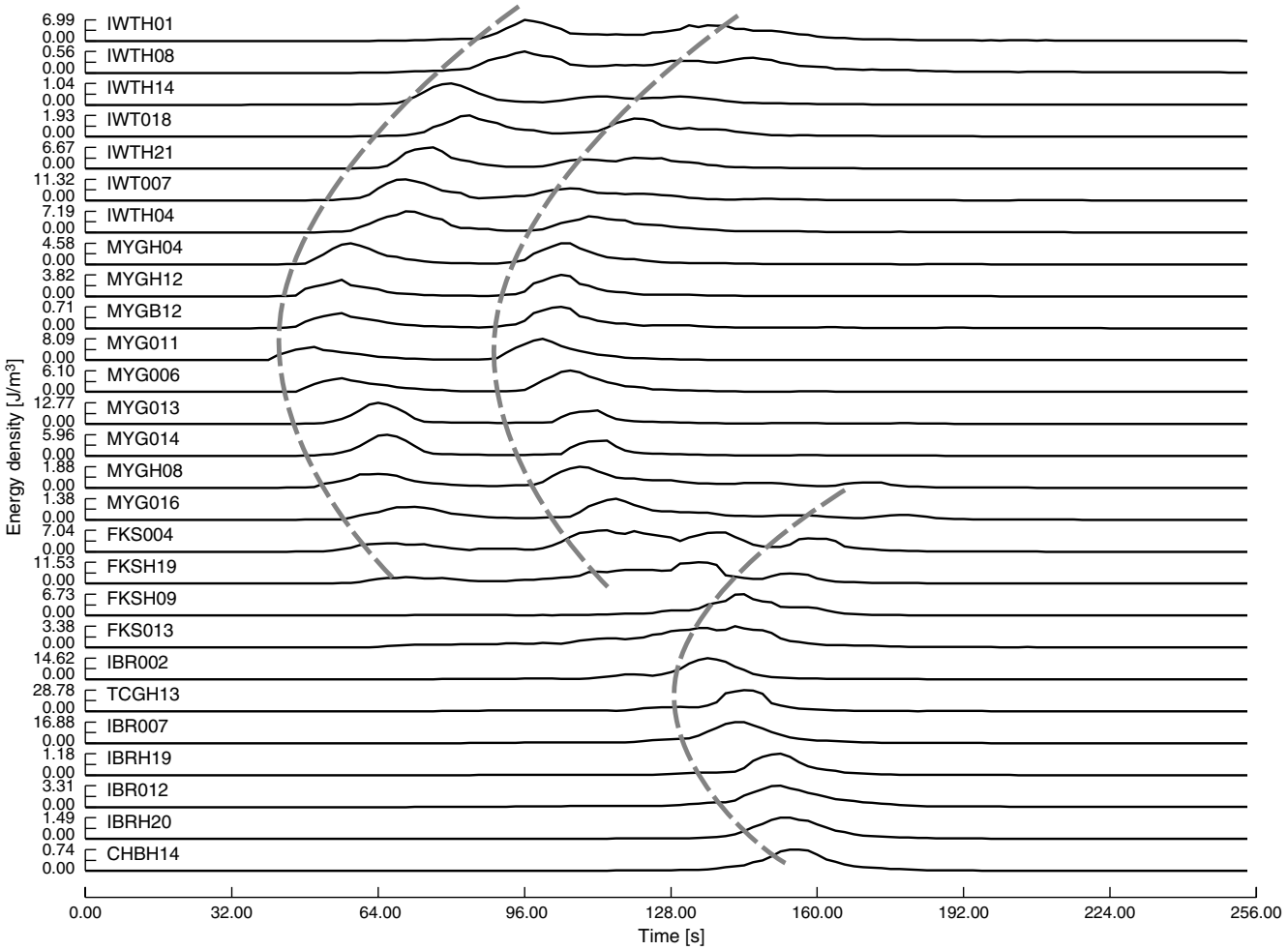

Figure 3 Observed seismogram envelopes in the 4–8 Hz band. Each envelope is normalized by the maximum amplitude at each station. They are aligned from top to bottom according to latitudes of the stations. Northern stations in Iwate and Miyagi prefectures shown on top clearly have two peaks. On the other hand, single peak is predominant at southern stations shown in the bottom of the panel. Three gray broken curves are handwritten to show onsets of the peaks.

travel times and takeoff angles are corrected in practice by using a horizontally layered velocity structure. I iteratively estimate the unknown parameters of W_k and S_i so as to minimize the residual between observed and synthesized envelopes. Suffix k stands for a subfault. However, because multiple time windows are set for each subfault, the total number of k is the number of the subfaults multiplied by the number of the time windows. A reference station has to be set to resolve a trade-off between W_k and S_i. Both the observed envelopes and the synthesized ones are normalized by the observed maximum value at each station to set the weights of all stations equal. Rupture velocity and a duration time of boxcar time function are estimated by grid search.

Data and Analysis

I analyze strong motion data from the mainshock recorded at 27 stations (solid triangles in Figure 1) of the National Research Institute for Earth Science and Disaster Prevention (NIED). These stations are within a hypocentral distance of 300 km. The top three characters of station codes IWT, MYG, FKS, IBR, TCG, and CHB stand for prefectures of Iwate, Miyagi, Fukushima, Ibaraki, Tochigi, and Chiba where the stations are located. Three-component acceleration records are sampled with a rate of 100 Hz. I first integrate original acceleration records into velocity records. Then I operate band-pass filters on the velocity records in three frequency bands of 1–2, 2–4, and 4–8 Hz. I then square the traces, sum up the three components, smooth them by a sliding boxcar time window of 10 s long, and multiply them with a mass density of 2.5 g/cm^3. The traces calculated in this way have a dimension of energy density (J/m^3). Envelopes used in this study are proportional to squared particle velocity amplitudes.

Envelopes calculated in the 4–8 Hz band are shown in Figure 3 according to station latitudes. Envelopes at northern stations in Iwate and Miyagi clearly show two peaks separated by about 60 s. On the other hand, the envelopes show a single peak at later times between 130 s and 160 s at southern

Table 1
Medium Parameters Estimated

Frequency (Hz)	Scattering g_0 (km^{-1})	Intrinsic (km^{-1})	Intrinsic Q
1–2	0.005	0.010	239.2
2–4	0.005	0.013	368.0
4–8	0.005	0.015	637.9

stations in Ibaraki and Chiba. In Fukushima, another small peak might exist around times of 130 s, but it is not as clear as the other peaks. Therefore, such direct observation suggests at least three subevents occurred during the mainshock rupture.

Time windows used for the inversion analysis are from *S*-wave onsets to a lapse time of 256 s. Because the envelope is resampled with an interval of 2 s for the inversion analysis, the number of data points for an envelope trace at a station is 128. The reference station is set at the subsurface receiver at station MYGH12, here denoted as MYGB12. This station was used as a reference in Nakahara (2008) because the site has an average *S*-wave velocity in the top 30 m depths exceeding 700 m/s.

I set a fault plane of the mainshock as shown in Figure 1. The strike and dip of the fault are set to be 195° and 13°, and its length and width are assumed to be 500 km and 200 km, respectively, with reference to Suzuki *et al.* (2011). I divide this fault plane into 40 subfaults, each of which is a 50 km × 50 km square. The focal mechanism on each subfault is assumed to be a strike of 195°, a dip of 13°, and a rake of 93°. At each subfault, eight boxcar time windows are set for energy radiation. Constant rupture velocity and the duration time are determined so as to minimize residuals between observed and synthesized envelopes.

Results

S-wave velocity of the medium is estimated at 3.94 km/s from arrival times of *S*-wave onsets. It is not an easy task to read *S*-wave onsets for large earthquakes, because they are masked by phases from later subevents. I read the *S*-wave onsets at the stations based on waveform similarities to initial *P* waves and theoretical travel times of *S* waves. Probably, errors of a few seconds remain in my pickings of the *S*-wave onsets at maximum. However, the errors will not affect the results significantly, because the envelopes are smoothed by 10-s-long windows and the size of each subfault is as large as 50 km × 50 km. The scattering parameters determined by the multiple lapse time window analysis (tabulated in Table 1) are used for calculating synthesized envelopes. Travel times and takeoff angles for the synthesized envelopes are corrected to improve the degree of fitting by using a velocity structure having six horizontal layers, which is slightly modified from Kato *et al.* (2003). In the inversion, a non-negative constraint of W_k is imposed by using the non-negative least-squares algorithm (Lawson and Hanson, 1974). Iteration is stopped after 1000 times, because residuals do not decrease significantly after further iterations.

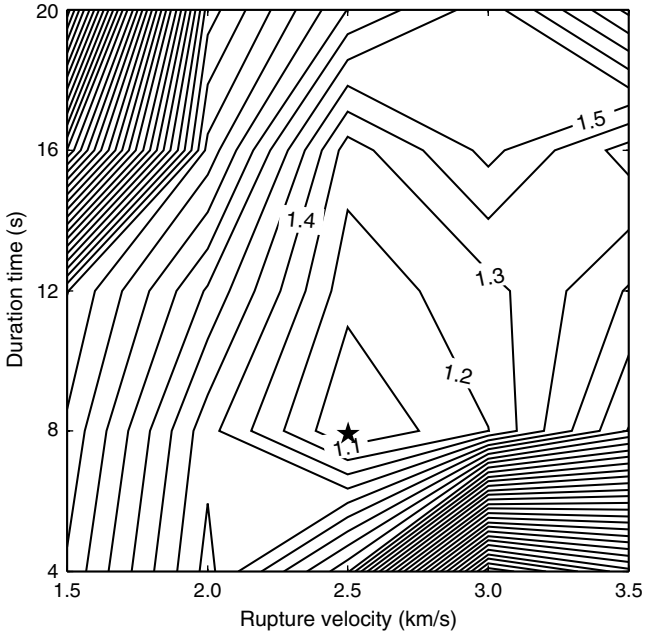

Figure 4 Residual map with respect to rupture velocity and the duration time of a boxcar time window for energy radiation in the 1–8 Hz band. Residuals for three frequency bands (1–2, 2–4, and 4–8 Hz) are summed up and normalized by the minimum value. A solid star marks the minimum residual point at the rupture velocity of 2.5 km/s and the duration time of 8 s.

I conduct the inversion in three frequency bands of 1–2, 2–4, and 4–8 Hz by changing the rupture velocity and the duration time. In Figure 4, I show the sum of residuals between observed and synthesized envelopes for all frequency bands in terms of rupture velocity and the duration time. Residuals shown are normalized by the minimum one. The best-fit parameters are the rupture velocity of 2.5 km/s and the duration of 8.0 s. This means that the rupture can take place for 64 s at each subfault because eight time windows are set for the subfault. Judging from the shape of the residuals, both parameters are well resolved.

Spatial distributions of energy radiation in 1–2, 2–4, 4–8, and 1–8 Hz are shown in Figure 5. Spatial patterns are not so different in different frequency bands. High-frequency energy is radiated mainly at greater depths close to the land. The strongest energy emanates from the second deepest subfault off Miyagi, shown by black. The second largest energy originates from the deepest subfault off Fukushima–Ibaraki border, shown by dark gray. Slight energy radiation is found at some of the shallowest subfaults only in the 2–4 Hz band, but not in the 1–2, and 4–8 Hz bands. I discuss the spatial resolution of the results later. Energies radiated from the entire fault are 2.3×10^{17} J for 1–2 Hz, 1.5×10^{17} J for 2–4 Hz, 4.1×10^{16} J for 4–8 Hz, and 4.2×10^{17} J in total for 1–8 Hz.

In Figure 6, I show snapshots of energy radiation from the fault every 10 s in the 4–8 Hz band. The amount of

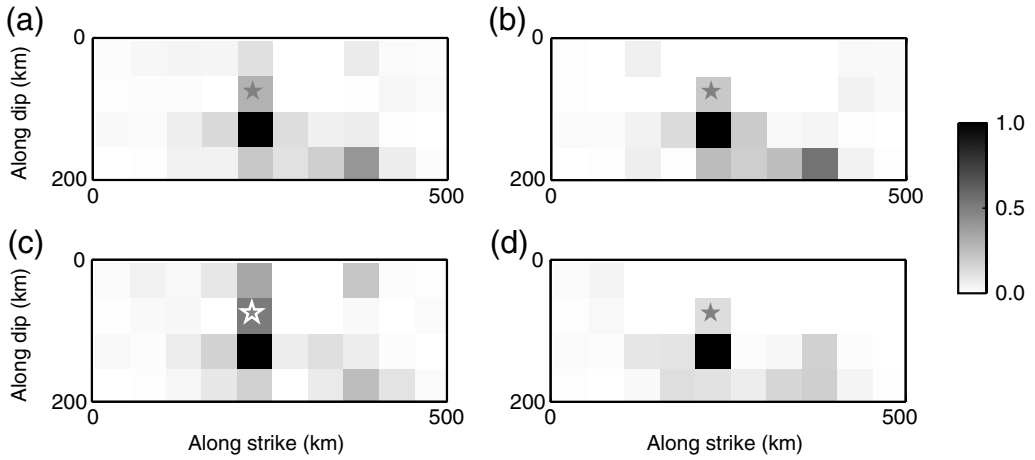

Figure 5 Spatial distribution of high-frequency energy radiation on the fault plane of 500 km long and 200 km wide for (a) 1–8, (b) 1–2, (c) 2–4, and (d) 4–8 Hz. A gray star shows the initial rupture point. Darker color means stronger energy radiation.

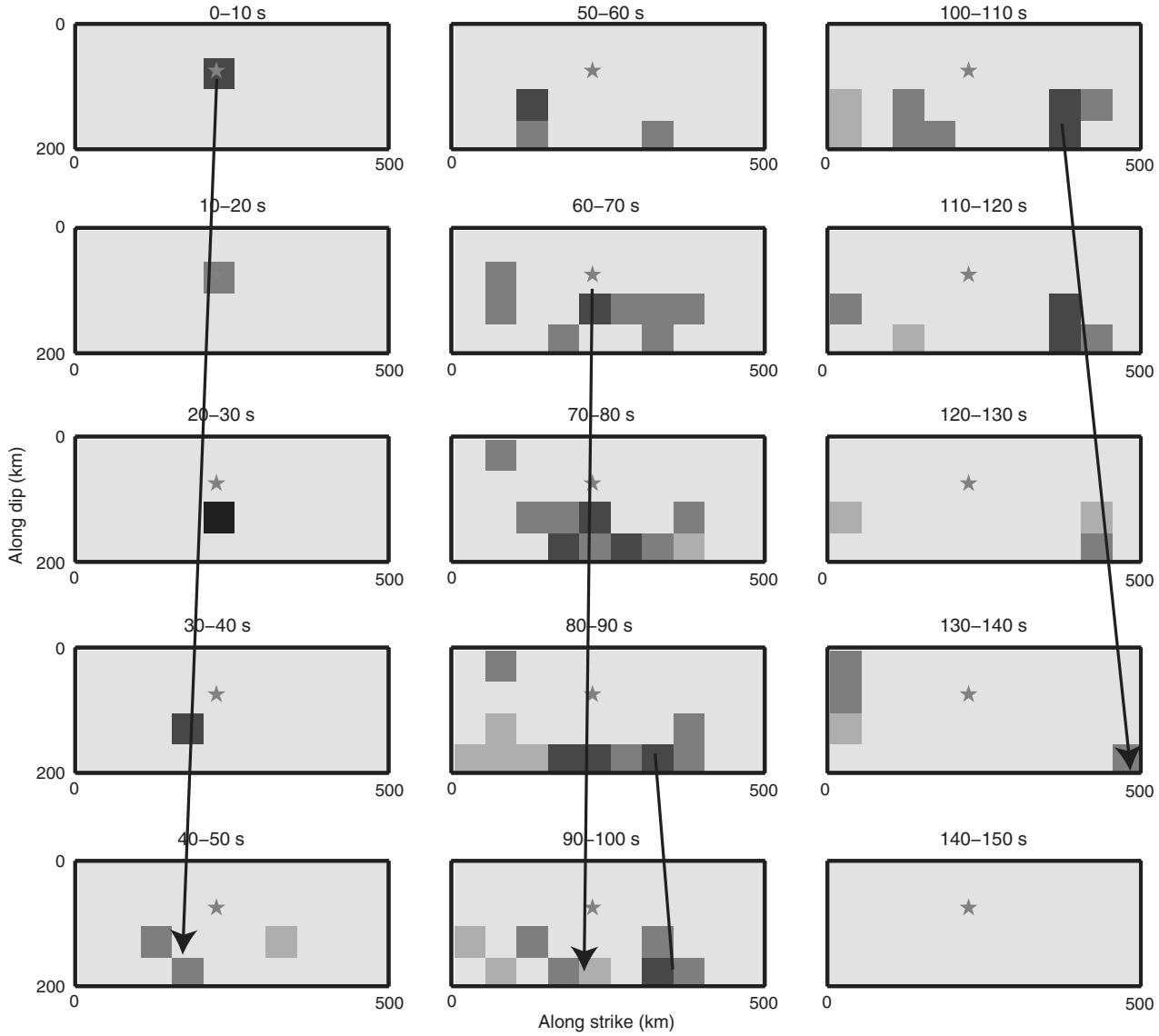

Figure 6 Snapshots of energy radiation in the 4–8 Hz band with a time step of 10 s. The amount of energy radiation shown is normalized by the maximum in all time steps. Three arrows show rupture propagation of the three subevents.

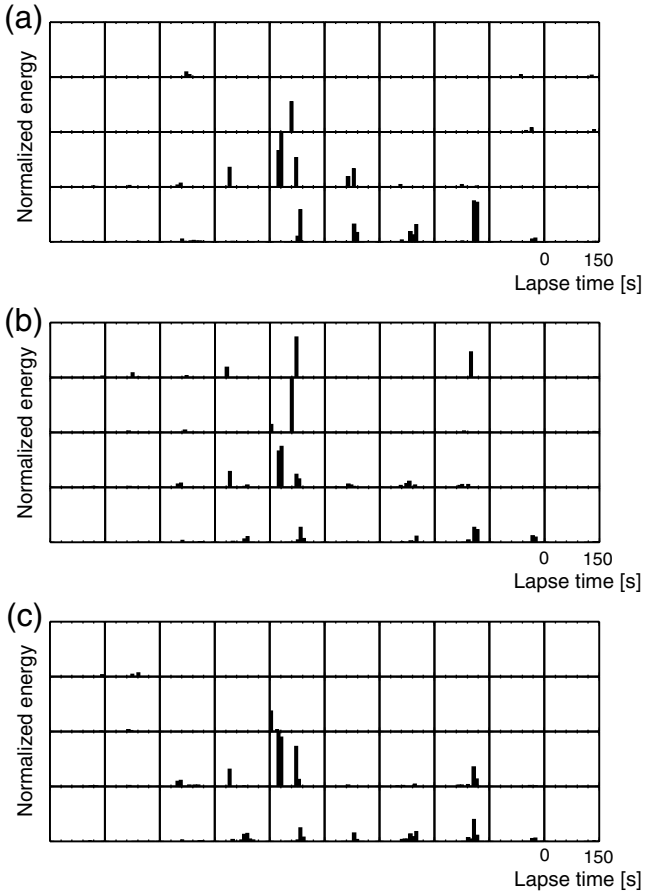

Figure 7 Spatiotemporal distribution of energy radiation at each subfault for three frequency bands of (a) 1–2, (b) 2–4, and (c) 4–8 Hz. Configuration of the subfaults is the same as Figures 5 and 6. Each small black column corresponds to energy radiation for an 8-s-long time window at each subfault. Amount of energy radiation is normalized by the maximum in each frequency band. Subfaults at greater depths off Miyagi clearly show energy radiation twice.

energy is normalized by the maximum value for all snapshots. In the first 60 s, energy radiation starts at the epicenter and propagates to the west landward as shown by an arrow. About 60 s later, the energy radiation restarts around the epicenter and then proceeds to the west for the next 50 s. The third radiation starts about 90 s later around off the Fukushima–Ibaraki border and propagates to the south. Snapshots in the 1–2, and 2–4 Hz bands are shown in Ⓔ Figures S1 and S2 in the electronic supplement to this article, respectively. In Figure 7, spatiotemporal distributions of energy radiation at each subfault are shown for three frequency bands of 1–2, 2–4, and 4–8 Hz. Each small black column corresponds to energy radiation for an 8-s-long time window at each subfault. Amount of energy radiation is normalized by the maximum in each frequency band. Energy radiation is clearly indentified twice at subfaults at greater depths off Miyagi for all three frequency bands. Contributions of three different frequency bands to the energy are shown with time in Figure 8. Lower frequencies have larger contributions. Temporal changes are similar for all three

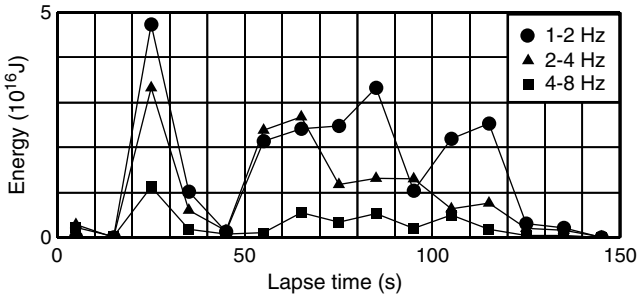

Figure 8 Temporal changes in energy radiation from the fault in three frequency bands of 1–2, 2–4, and 4–8 Hz shown by solid circles, solid triangles, and solid squares, respectively. Lower frequency shows larger contributions.

frequency bands, showing three bursts at lapse times of about 30, 60–90, and 110 s.

In Figure 9, comparison between the observed envelopes (solid curves) and the synthesized ones (broken curves) is shown. The envelopes match each other well. I am able to relate each peak and each energy burst shown in Figure 6. The first and the second bursts of energy radiation off Miyagi correspond to the first and the second peaks on the envelopes at the northern stations, respectively. The third burst of energy off the Fukushima–Ibaraki border explains the single peak on the envelopes at the southern stations.

Discussion

In order to check the spatial resolution of my inversion results, I conduct a checkerboard resolution test. The left panel in Figure 10 is an input model in which strong energy radiation is shown by black. Recall that each subfault is a 50 km × 50 km square. Synthetic envelopes are calculated for the input model and 1% random noises obeying an exponential distribution are added. The exponential distribution originates from the mean-squared envelope of a Gaussian random noise trace. For the statistics of seismogram envelopes, readers can refer to Nakahara and Carcolé (2010). I then conduct the inversion using the noise-added envelopes to obtain the result shown in the right panel. The input pattern is well reproduced at greater depths close to the land. On the other hand, the input pattern cannot be restored at shallower parts and the northern edges which are far from the stations on land. However, the amount of energy is more or less the same as the input energy. Therefore, I judge that the amount of energy radiation can be correctly estimated, though the spatial resolution is low at shallower depths.

In Figure 11, I compare the envelope inversion results with a result of Nakahara *et al.* (2011) which directly observed rupture propagation of the Tohoku-Oki earthquake in 0.5–2.0 Hz using a near-field small seismic array. They were capable of resolving rupture propagation in the along-strike direction but not in the along-dip direction from back azimuths of incident phases on the array estimated by a semblance analysis, and identified four bursts of energy in the

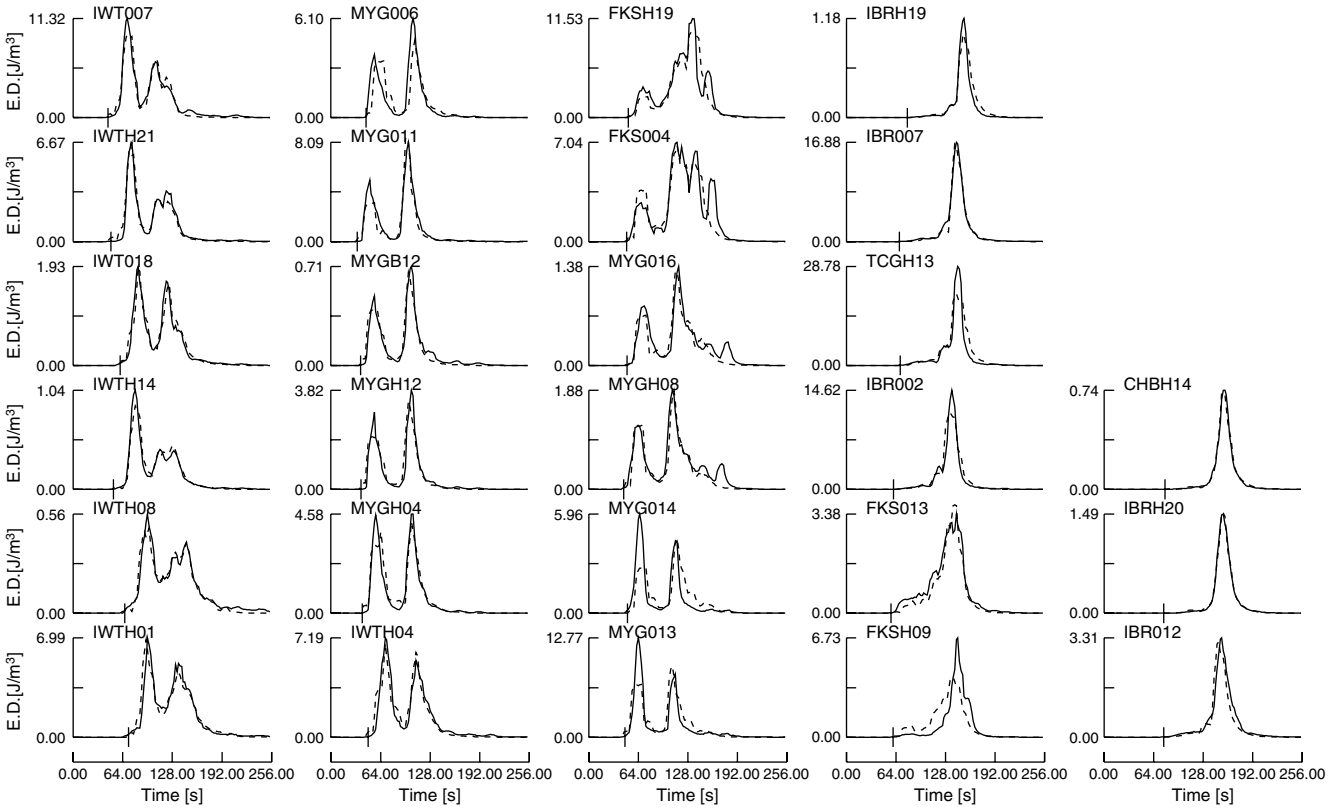

Figure 9 Matches between observed (solid curves) and synthesized (broken curves) envelopes in the 4–8 Hz band. Data in lapse times from the *S*-wave onset to a lapse time of 256 s are used for the inversion analysis. *S*-wave onset times are shown by short solid vertical lines.

frequency band as shown by ellipses in Figure 11b. The energy radiation in the 1–2 Hz band estimated in this study is projected to the linear fault shown in Figure 11a, and is shown in Figure 11c. The first two bursts in Figure 11b contribute to the strongest energy radiation off Miyagi in Figure 11c, and the third burst corresponds to the second largest energy radiation off the Fukushima–Ibaraki border. In this way, both results are mainly compatible with each other, but the fourth burst detected by the array is not found by the envelope inversion. Because the array analysis deals with semblance, a measure of coherence neglecting amplitude, the fourth burst may be coherent but too weak in energy to be detected by the envelope inversion.

Scaling relations of high-frequency seismic energy radiation in octave-width frequency bands are shown with respect to moment magnitude in Figure 12. Open circles, open triangles, and open squares are observed energy for 1–2, 2–4, and 4–8 Hz, respectively. Three solid lines show empirical relations for 1–2, 2–4, and 4–8 Hz (from top to bottom in the figure) derived from offshore earthquakes in northeastern Japan by Nakahara (2008). The lines mean that the logarithm of high-frequency energy in a frequency band is proportional to the moment magnitude with a factor of 1, and this relation is expected based on the omega-squared source spectrum and constant stress drops (Nakahara, 2008). The gray symbols are estimated for the Tohoku-Oki earthquake. In terms of

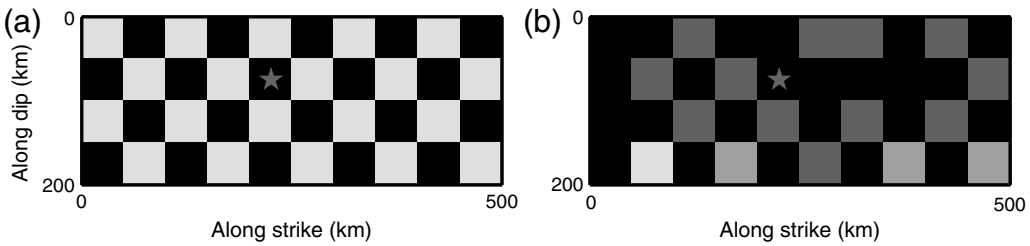

Figure 10 Checkerboard resolution test in the 4–8 Hz band. Panel (a) is the input model and panel (b) shows the reconstructed image by the inversion of noise-added synthetic envelopes from the input model. Spatial resolution is found to be high at greater depths and low at shallower depths.

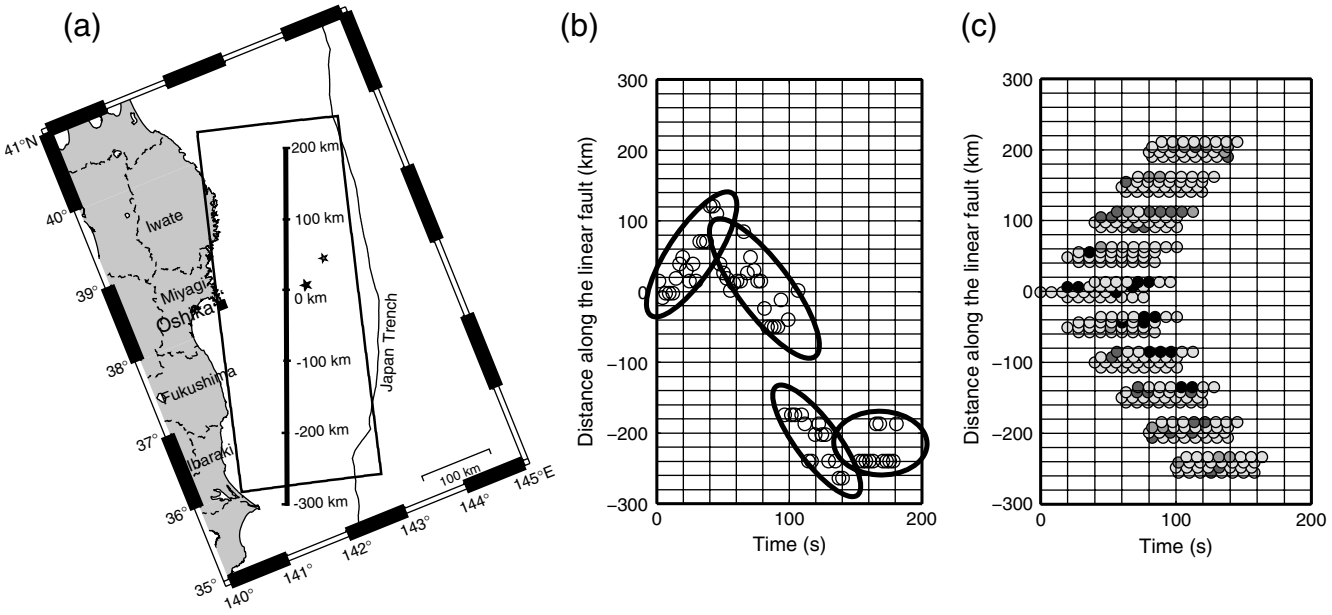

Figure 11 Comparison between the results of this study with those of Nakahara *et al.* (2011). (a) Location of the Oshika array is shown by a solid square. The linear fault to which the rupture propagation is projected back is shown by a thick solid line. A solid star and a small grey star are the epicenters of the Tohoku-Oki earthquake and the 9 March foreshock, respectively. (b) Rupture propagation of the Tohoku-Oki earthquake along the linear fault estimated from back azimuths of the incident phases on the array. Four bursts of energy identified are shown by ellipses. (c) Projection of high-frequency energy radiation in the 1–2 Hz estimated by this study to the linear fault. Darker circles show stronger energy radiation.

high-frequency radiation, the Tohoku-Oki earthquake is smaller for an M_w 9.0 earthquake in northeastern Japan, corresponding to 8.6–8.7 according to the empirical relations.

Here, I discuss a relation between low-frequency radiation areas with high-frequency radiation areas. This issue is important for predicting strong ground motion from future earthquakes in broad frequency bands, and is interesting as well in terms of rupture dynamics. Nakahara (2008) summarized the relation for moderate to large earthquakes. He classified the relation as complementary or otherwise. Complementary means that high-frequency waves are radiated from different areas, usually peripheries, of low-frequency radiation areas, which is expected for a crack-like rupture (e.g., Madariaga, 1976; Kato, 2007). Among about 15 earthquakes, 6 show the complementary relation. However the other earthquakes do not show the complementary relation, suggesting that heterogeneities in stress, strength, and/or ambient structures may play a role.

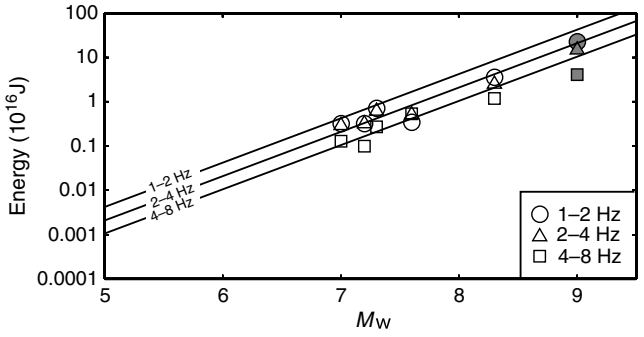

Figure 12 Scaling relation of high-frequency seismic energy in octave-width frequency bands with respect to moment magnitude. Open circles, open triangles, and open squares are observed energy for 1–2, 2–4, and 4–8 Hz, respectively. Three solid lines with a proportionality factor of 1 show empirical relations derived for 1–2, 2–4, and 4–8 Hz from offshore earthquakes in northeastern Japan by Nakahara (2008). The gray symbols are estimated for the Tohoku–Oki earthquake.

I consider the relation for the Tohoku-Oki earthquake too by comparing my results with other studies estimating slip distribution on the fault in lower frequencies. Suzuki *et al.* (2011) used near-field strong-motion records at 36 stations and determined the spatiotemporal slip distribution by waveform inversions in the frequency band of 0.01–0.125 Hz, which is much lower than the 1–8 Hz analyzed in this study. Because data set and fault geometries are similar between Suzuki *et al.* (2011) and this study, I compare their slip distribution with the energy distribution in this study, as shown in Figure 13. The top panel shows the slip distribution by Suzuki *et al.* (2011), displaying the maximum slip of 48 m at shallower depths near the trench off Miyagi. Large amount of slip at shallower depths was also estimated by many studies from inversions of tsunami records (e.g., Fujii *et al.*, 2011) and more directly from bathymetric changes measured close to the trench axis before and after the Tohoku-Oki earthquake (Fujiwara *et al.*, 2011), though discrepancies in slip models are still found (e.g., Koketsu *et al.*, 2011). On the other hand, high-frequency seismic energy was radiated from greater depths shown in the bottom panel. Because areas of strong low-frequency radiation do not overlap with those of

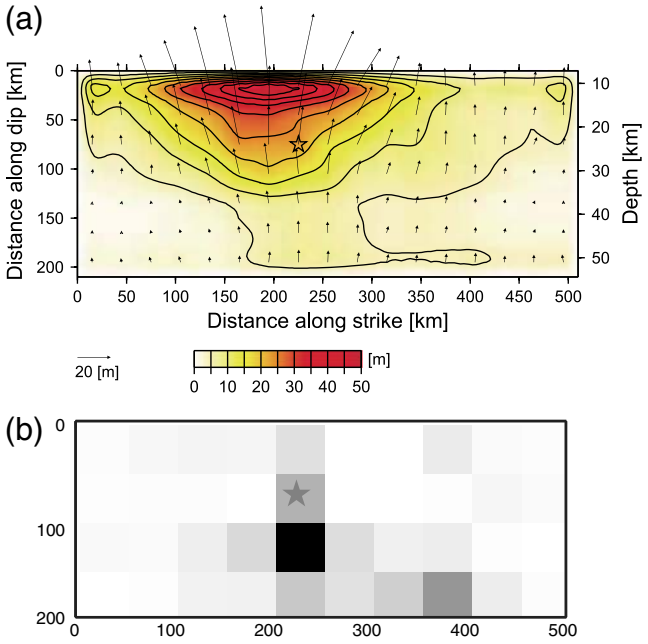

Figure 13 (a) Spatial distribution of slip on the fault plane estimated from inversion of near-field strong-motion data by Suzuki *et al.* (2011). The fault model has a size of 510 km in length and 210 km in width. Darker shade corresponds to larger slip. An open star is the location of the initial rupture point. (b) Spatial distribution of high-frequency energy radiation for 1–8 Hz is shown in a gray scale. Darker color corresponds to strong energy radiation. The color version of this figure is available only in the electronic edition.

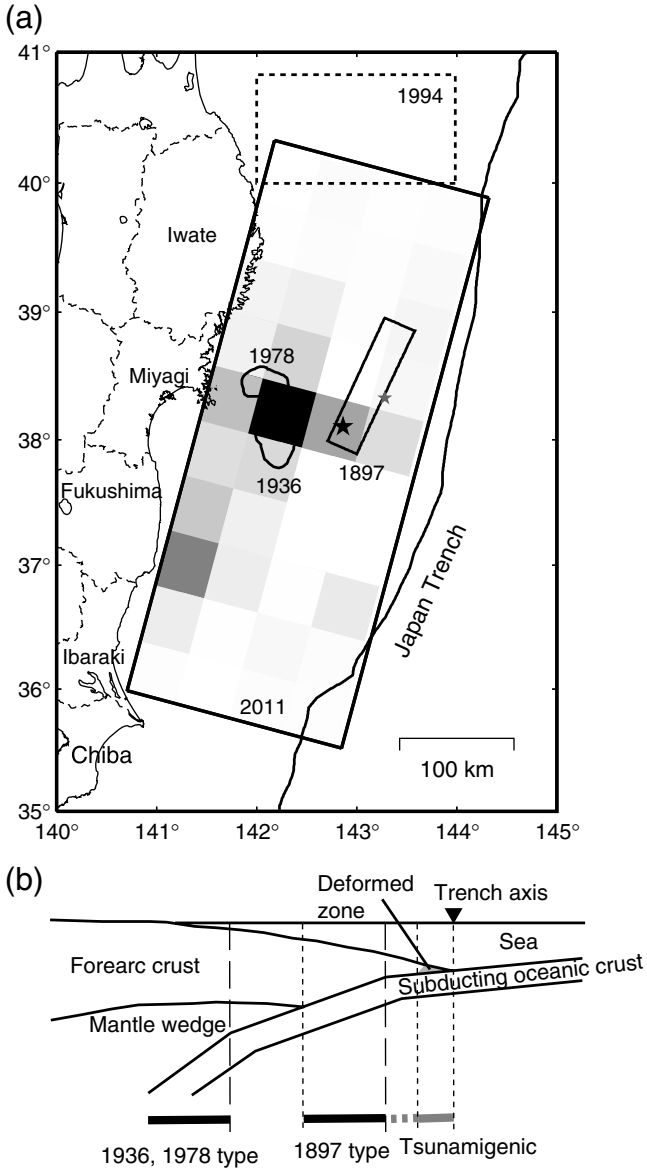

Figure 14 (a) Spatial distribution of energy radiation in 1–8 Hz estimated in this study is shown in gray scale. Three previous earthquakes off Miyagi are shown by solid curves: asperities of the 1936 and the 1978 earthquakes (Yamanaka and Kikuchi, 2004), and the source area of the tsunami for the 1897 earthquake (Aida, 1977). The solid and gray stars denote the epicenters of the Tohoku–Oki earthquake and the 9 March foreshock, respectively. The source region of the 1994 Sanriku–Haruka–Oki earthquake (Nakahara *et al.*, 1998) is shown by a dotted rectangle. (b) Schematic illustration of the structure off Miyagi based on Miura *et al.* (2005) and Ito *et al.* (2005). Changes in dip angles of the subducting plate and materials composing the overriding plate may control rupture characteristics of large earthquakes off Miyagi.

strong high-frequency radiation, the relation is classified as complementary.

Areas of strong high-frequency energy radiation from the Tohoku-Oki earthquake seem to have a good correlation with along-dip segmentations off Miyagi. Large earthquakes have repeatedly occurred off Miyagi. Source regions (asperities) of two recent earthquakes in 1936 and 1978 estimated by Yamanaka and Kikuchi (2004) are shown by solid curves in Figure 14a. The events occurred at greater depths and generated strong ground motions (e.g., Kanda and Takemura, 2005). On the other hand, the 5 August 1897 earthquake took place at shallower depths, shown by a solid rectangle, and was known to generate larger tsunamis but weaker ground motions compared with the two earthquakes in 1936 and 1978 (e.g., Aida, 1977; Kanda and Takemura, 2005). As shown in Figure 14b, Miura *et al.* (2005) pointed out that the shallow-most part farther to the east of the 1897-type source region is aseismic or tsunamigenic. Some studies proposed that these segmentations are controlled by geometries (i.e., dip angles) of the subducting plate (e.g., Ito *et al.*, 2005) or structural changes such as a deformed zone, forearc crust, and wedge mantle (e.g., Miura *et al.*, 2005). Yamamoto *et al.* (2008) showed that the V_P/V_S ratio in the wedge mantle above the 1978 source region is low, suggesting that the wedge mantle is not serpentinized. According to the envelope inversion in this study, high-frequency radiation off Miyagi is estimated to be very large in the 1936- and 1978-type source regions, modest in the 1897-type source region, and weak to the farther east. Such a structural difference might be a controlling factor for the frequency-dependent rupture of the Tohoku-Oki earthquake. In terms of the classification recently proposed by Lay *et al.* (2012), the 1936- and 1978-type source

regions correspond to domain C and the 1897-type source region corresponds to domain B.

Just north of the source area of the Tohoku-Oki earthquake (a dotted rectangle in Figure 14a), the 1994 Sanriku–Haruka-Oki earthquake (M_w 7.7) took place. This earthquake also exhibited a clear frequency dependence of rupture characteristics (e.g., Sato *et al.*, 1996; Nakahara *et al.*, 1998). The rupture propagated from the east to the west. Large slip was estimated around the center of the fault plane in lower frequencies, but high-frequency waves were strongly radiated from the western edge at greater depths. The rupture of this earthquake did not reach to the trench axis, and only small tsunamis were generated accordingly. Therefore, this earthquake probably ruptured domains B and C of the classification by Lay *et al.* (2012). Detailed comparison of the rupture characteristics with the geometry of the plate interface and velocity structures will be necessary in this region too.

Finally, I mention problems and limitations of my inversion analysis. The first point is about the fault geometry. Though the linear fault model of Suzuki *et al.* (2011) with a dip angle of 13° is used in this study, dip angles of the plate interface are known to increase from the east to the west in reality. I do not take this effect in the inversion analysis, mainly because I put more emphasis on using the same fault geometry as the published model of Suzuki *et al.* (2011). But here I make rough estimations of the effect. The dip angle increases up to 23° to the deeper part of the fault according to Miura *et al.* (2005). So I change dip angles of the deepest two columns of the subfaults from 13° to 23° as an example. Accordingly, the depths of the subfaults become deeper by 6 km at maximum. This slightly affects the radiation pattern of *S* waves and delays *S*-wave travel times by up to 1.1 s on average (2.9 s at maximum) compared with the linear fault model. But such differences in the *S*-wave travel times do not have significant effects on the results, based on the same reasoning made for the picking errors in *S*-wave travel times. The second point is regarding how to synthesize envelope Green's functions. Only *S* waves are considered in the modeling by neglecting *P* waves and surface waves which are present in the observed envelopes. Because *P*-wave energy is known to be about 4.3% (= 1/23.4) of *S*-wave energy for a double-couple source, contribution of *P* waves may be neglected to an accuracy of about 5%. On the other hand, contribution of surface waves is expected to be larger for sources at shallow depths and in lower frequencies. So this probably affects the estimates of radiated energy in this study. In the MLTWA analysis, scattering parameters are estimated so that synthesized envelopes explain observed envelopes, even if only *S* waves are considered in the modeling. This partly compensates for the effect of surface waves, but this also renders physical meanings of the scattering parameters unclear. In higher frequencies than about 5 Hz, contribution of surface waves becomes very weak in *S*-wave coda, which was clarified by modeling energy partitioning of borehole records from small local earthquakes off Iwate by Nakahara and Margerin (2011). They speculated that high-frequency surface waves may be attenuated due to strong attenuation at shallower depths. But it is not easy so far to evaluate the contributions of surface waves quantitatively. Therefore, I only note that my estimates of radiated energy in high frequencies, especially in 1–2 and 2–4 Hz, are partly contaminated by surface waves. It is necessary to include surface waves in the modeling of envelopes, though it is still a challenge (e.g., Maeda *et al.*, 2008).

Conclusion

I have estimated the spatial distribution of high-frequency energy radiation on the fault of the 2011 Tohoku-Oki earthquake by applying the envelope inversion method of Nakahara *et al.* (1998) to 27 near-field strong-motion records. Envelope Green's functions were synthesized with the scattering parameters estimated from 13 aftershocks. I then conducted the source inversion in three frequency bands of 1–2, 2–4, and 4–8 Hz, and estimated the spatial distribution of high-frequency energy radiation on the fault of 500 km × 200 km. Rupture velocity and the duration time of energy radiation were determined by a grid search at 2.5 km/s and 8.0 s, respectively. The energy amounts from the entire fault plane were estimated as 2.3×10^{17} J for 1–2 Hz, 1.5×10^{17} J for 2–4 Hz, 4.1×10^{16} J for 4–8 Hz, and 4.2×10^{17} J in total for 1–8 Hz. The inversion revealed two regions of strong high-frequency energy radiation on the fault plane: at greater depths off Miyagi and off the Fukushima–Ibaraki border. Bursts of high-frequency energy radiation took place two times off Miyagi, corresponding to two peaks observed at the northern stations. Another burst occurred later off the Ibaraki–Fukushima border, explaining the single peak found at the southern stations. Areas of strong high-frequency energy radiation are located at greater depths and seem to have a good correlation with segmentations along the dip direction, which suggests that a structure around the source region may control the strong high-frequency energy radiation.

Data and Resources

Seismograms used in this study can be obtained from K-NET and KiK-net, National Research Institute for Earth Science and Disaster Prevention, Tsukuba, Japan at http://www.kyoshin.bosai.go.jp/cgi-bin/kyoshin/menu_en.cgi (last accessed April 2012). Figures were prepared using Generic Mapping Tools (Wessel and Smith, 1998).

Acknowledgments

Seismograms recorded by K-NET, KiK-net, and F-net managed by the National Research Institute for Earth Science and Disaster Prevention (NIED) were used in this study. The author is grateful to Wataru Suzuki, NIED, for providing a figure of his slip model. Constructive comments from the editor, M. Bouchon, and two anonymous reviewers are greatly appreciated.

References

AGU (American Geophysical Union) (2012). The 11 March 2011 Tohoku-Oki Earthquake and Tsunami, *Geophys. Res. Lett.* **39,** no. 7.

Aida, I. (1977). Simulations of large tsunamis occurring in the past off the coast of the Sanriku District, *Bull. Earthq. Res. Inst.* **52,** 71–101.

Fehler, M., M. Hoshiba, H. Sato, and K. Obara (1992). Separation of scattering and intrinsic attenuation for the Kanto–Tokai region, Japan using measurements of *S*-wave energy vs. hypocentral distance, *Geophys. J. Int.* **108,** 787–800.

Fire and Disaster Management Agency (2012). The 2011 Off the Pacific Coast of Tohoku earthquake (The 145th report), http://www.fdma.go.jp/bn/2012/detail/691.html (last accessed April 2012).

Fujii, Y., K. Satake, S. Sakai, M. Shinohara, and T. Kanazawa (2011). Tsunami source of the 2011 Off the Pacific Coast of Tohoku earthquake, *Earth Planets Space* **63,** 815–820.

Fujiwara, T., S. Kodaira, T. No, Y. Kaiho, N. Takahashi, and Y. Kaneda (2011). The 2011 Tohoku-Oki earthquake: Displacement reaching the trench axis, *Science* **334,** 1,240.

Gusev, A. A., and V. M. Pavlov (1991). Deconvolution of squared velocity waveform as applied to the study of a noncoherent short-period radiator in the earthquake source, *Pure Appl. Geophys.* **136,** 235–244.

Ide, S., A. Baltay, and G. C. Beroza (2011). Shallow dynamic overshoot and energetic deep rupture in the 2011 M_w 9.0 Tohoku-Oki earthquake, *Science* **332,** 1,426–1,429, doi: 10.1126/science.1207020.

Ito, A., G. Fujie, S. Miura, S. Kodaira, Y. Kaneda, and R. Hino (2005). Bending of the subducting oceanic plate and its implication for rupture propagation of large interplate earthquakes off Miyagi, Japan, in the Japan Trench subduction zone, *Geophys. Res. Lett.* **32,** L05310, doi: 10.1029/2004gl022307.

Kakehi, K., and K. Irikura (1996). Estimation of high-frequency wave radiation areas on the fault plane by the envelope inversion of acceleration seismograms, *Geophys. J. Int.* **125,** 892–900.

Kanda, K., and M. Takemura (2005). Verification of the sequence of disastrous earthquakes off Miyagi Prefecture based on seismic intensity data, *Zisin 2* **58,** 177–198.

Kato, N. (2007). How frictional properties lead to either rupture-front focusing or cracklike behavior, *Bull. Seismol. Soc. Am.* **97,** 2182–2189.

Kato, K., M. Takemura, and T. Ikeura (2003). Asperity and its effect on near-fault strong motions during the 1978 Miyagi-ken-Oki earthquake—Study on the basis of waveform inversion analysis, Summaries of Technical Papers of Annual Convention, Architectural Institute of Japan, 21,068.

Kiser, E., and M. Ishii (2012). The March 11, 2011 Tohoku-Oki earthquake and cascading failure of the plate interface, *Geophys. Res. Lett.* **39,** L00G25, doi: 10.1029/2012GL051170.

Koketsu, K., Y. Yokota, N. Nishimura, Y. Yagi, S. Miyazaki, K. Satake, Y. Fujii, H. Miyake, S. Sakai, Y. Yamanaka, and T. Okada (2011). A unified source model for the 2011 Tohoku earthquake, *Earth Planet. Sci. Lett.* **310,** 480–487.

Koper, K. D., A. R. Hutko, T. Lay, C. J. Ammon, and H. Kanamori (2011). Frequency-dependent rupture process of the 2011 M_w 9.0 Tohoku earthquake: comparison of short-period *P* wave backprojection images and broadband seismic rupture models, *Earth Planets Space* **63,** 599–602.

Kurahashi, S., and K. Irikura (2011). Source model for generating strong ground motions during the 2011 Off the Pacific Coast of Tohoku earthquake, *Earth Planets Space* **63,** 571–576.

Lawson, C. L., and R. J. Hanson (1974). *Solving Least Squares Problems*, Prentice-Hall, Inc., Englewood Cliffs, New Jersey, 340 pp.

Lay, T., H. Kanamori, C. J. Ammon, K. D. Koper, A. R. Hutko, L. Ye, H. Yue, and T. M. Rushing (2012). Depth-varying rupture properties of subduction zone megathrust faults, *J. Geophys. Res.* **117,** doi: 10.1029/2011JB009133.

Madariaga, R. (1976). Dynamics of an expanding circular fault, *Bull. Seismol. Soc. Am.* **66,** 639–666.

Maeda, T., H. Sato, and T. Nishimura (2008). Synthesis of coda wave envelopes in randomly inhomogeneous elastic media in a half-space: Single scattering model including Rayleigh waves, *Geophys. J. Int.* **172,** 130–154.

Miura, S., N. Takahashi, A. Nakanishi, T. Tsuru, S. Kodaira, and Y. Kaneda (2005). Structural characteristics off Miyagi forearc region, the Japan Trench seismogenic zone, deduced from a wide-angle reflection and refraction study, *Tectonophysics* **407,** 165–188.

Nakahara, H. (2008). Seismogram envelope inversion for high-frequency seismic energy radiation from moderate to large earthquakes, *Adv. Geophy.* **50,** 401–426.

Nakahara, H., and E. Carcolé (2010). Maximum-likelihood method for estimating coda *Q* and the Nakagami-*m* parameter, *Bull. Seismol. Soc. Am.* **100,** 3174–3182.

Nakahara, H., and L. Margerin (2011). Testing equipartition for *S*-wave coda using borehole records of local earthquakes, *Bull. Seismol. Soc. Am.* **101,** 2243–2251.

Nakahara, H., T. Nishimura, H. Sato, and M. Ohtake (1998). Seismogram envelope inversion for the spatial distribution of high-frequency energy radiation from the earthquake fault: Application to the 1994 far east off Sanriku earthquake, Japan, *J. Geophys. Res.* **103,** 855–867.

Nakahara, H., H. Sato, T. Nishimura, and H. Fujiwara (2011). Direct observation of rupture propagation during the 2011 Off the Pacific Coast of Tohoku, Japan, earthquake (M_w 9.0) using a small seismic array, *Earth Planets Space* **63,** 589–594.

Sato, T., K. Imanishi, and M. Kosuga (1996). Three-stage rupture process of the 28 December 1994 Sanriku-Oki earthquake, *Geophys. Res. Lett.* **23,** 33–36.

Sato, H., H. Nakahara, and M. Ohtake (1997). Synthesis of scattered energy density for the non-spherical radiation from a point shear dislocation source based on the radiative transfer theory, *Phys. Earth Planet. In.* **104,** 1–13.

Simons, M., S. E. Minson, A. Sladen, F. Ortega, J. Jiang, S. E. Owen, L. Meng, J.-P. Ampuero, S. Wei, R. Chu, D. V. Helmberger, H. Kanamori, E. Hetland, A. W. Moore, and F. H. Webb (2011). The 2011 magnitude 9.0 Tohoku-Oki earthquake: Mosaicking the megathrust from seconds to centuries, *Science* **332,** 1421–1425, doi: 10.1126/science.1206731.

Suzuki, W., S. Aoi, H. Sekiguchi, and T. Kunugi (2011). Rupture process of the 2011 Tohoku-Oki mega-thrust earthquake (*M* 9.0) inverted from strong-motion data, *Geophys. Res. Lett.* **38,** L00G16, doi: 10.1029/2011GL049136.

Wessel, P., and W. H. F. Smith (1998). New improved version of the Generic Mapping Tools released, *Eos Trans. AGU* **79,** 579.

Yamamoto, Y., R. Hino, K. Suzuki, Y. Ito, T. Yamada, M. Shinohara, T. Kanazawa, G. Aoki, M. Tanaka, K. Uehira, G. Fujie, Y. Kaneda, T. Takanami, and T. Sato (2008). Spatial heterogeneity of the mantle wedge structure and interplate coupling in the NE Japan forearc region, *Geophys. Res. Lett.* **35,** L23304, doi: 10.1029/2008gl036100.

Yamanaka, Y., and M. Kikuchi (2004). Asperity map along the subduction zone in northeastern Japan inferred from regional seismic data, *J. Geophys. Res.* **109,** B07307, doi: 10.1029/2003JB002683.

Yomogida, K. and H. Kanamori (Editors) (2011). *First Results of the 2011 Off the Pacific Coast of Tohoku Earthquake, Earth, Planets and Space*, 63, no. 7, 511–902.

Zeng, Y., K. Aki, and T.-L. Teng (1993). Mapping of the high-frequency source radiation for the Loma Prieta earthquake, California, *J. Geophys. Res.* **98,** 11,981–11,993.

Appendix

Estimation of Scattering Parameters Based on the Multiple Lapse Time Window Analysis

Total attenuation is the sum of intrinsic absorption and scattering attenuation. The two factors can be separately

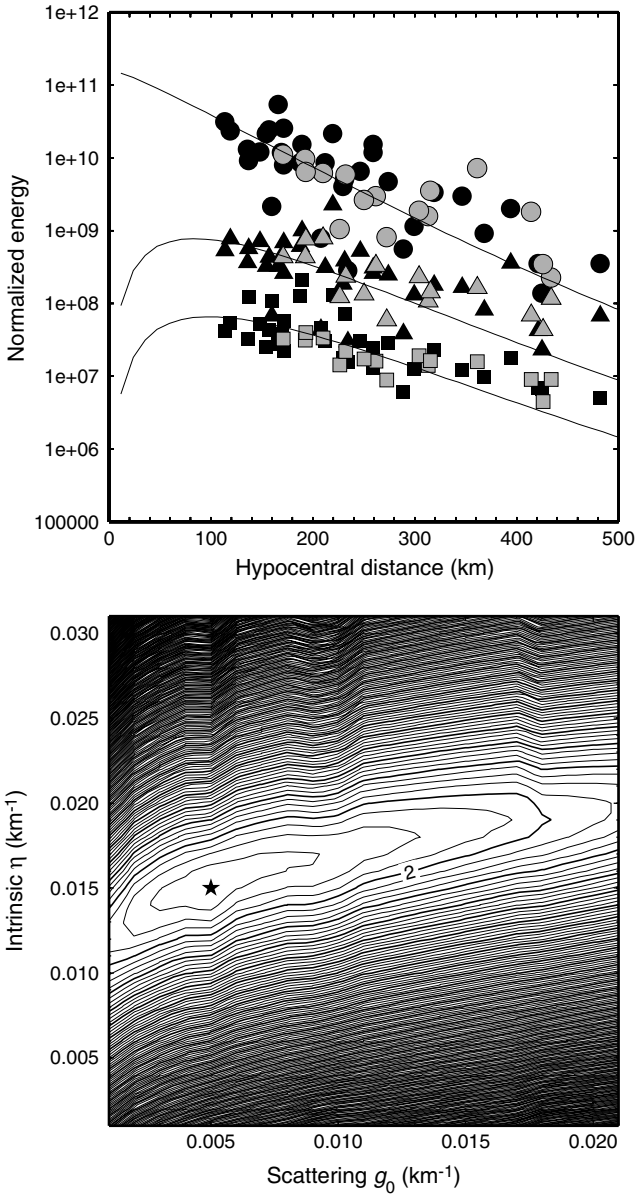

Figure A1 Results obtained by the multiple lapse time window analysis for 4–8 Hz. Top panel shows the coda-normalized and geometrical-spreading corrected energy integrals versus hypocentral distance for the first, the second, and the third time windows by solid circles, solid triangles, and solid squares, respectively. Results for the earthquakes with longitudes larger than 143 °E are shown by gray symbols. Solid lines are the best fit theoretical values for these three quantities. Bottom panel shows contour curves of residuals between the observed and the theoretical energy integrals for g_0 and η. Residuals are normalized by the minimum one, and are shown with a contour interval of 0.1. A solid star marks the location of the minimum residual.

estimated by the multiple lapse time window analysis (Fehler *et al.*, 1992). I select three successive time windows of 30-s length on a seismogram starting from the *S*-wave onset t_s. I denote $E_1(f;r)$ as the integral of the squared velocity records over the first time window. Similarly, $E_2(f;r)$ and $E_3(f;r)$ are defined for the second and the third time windows, respectively. I calculate coda power $E_c(f;r)$ as an integral of squared velocity records for an octave frequency band with a center frequency of f Hz at lapse times between 165 and 175 s. The magnitude difference of events and site amplification factors can be corrected based on the idea of the coda normalization method. The energy integrals normalized by the coda energy are further corrected for a geometrical spreading factor. The residuals of the normalized energy integrals between syntheses and observations have to be minimized by the grid search to estimate scattering coefficient g_0 and intrinsic absorption coefficient η. A step of the search is 0.001 km^{-1} for the parameters.

Seismograms from thirteen aftershocks (gray stars in Fig. 1) recorded at six F-net stations (gray triangles in Fig. 1) are used in the analysis. The fit between the synthetic normalized energy integrals and the observed ones in 4–8 Hz band is shown in the top panel in Figure A1. Especially, the results for three earthquakes with longitudes of larger than 143 °E are shown by gray symbols. Within the range of variations in data, any systematic differences between those earthquakes and the others are not found. The residuals between syntheses and observations are shown with respect to g_0 and η. A star marks the best-fit parameters. The results in the 1–2, and 2–4 Hz bands are shown in Ⓔ Figures S3 and S4 in the electronic supplement to this article. All the results are tabulated in Table 1. The scattering parameters are 0.005 km^{-1}, a reciprocal of which is a scattering mean free path of 200 km. This means that seismic energy is scattered once every 200 km on average during propagation. The mean free path divided by *S*-wave velocity is called mean free time. *S*-wave velocity of 3.94 km/s roughly gives the mean free time of 50 s, which means that a scattering takes place every 50 s. Energies can be scattered up to five times during the time window of the envelope inversion up to a lapse time of 256 s, suggesting the importance of multiple scattering for this case.

Department of Geophysics, Graduate School of Science
Tohoku University
6-3, Aramaki-Aza-Aoba
Aoba-ku, Sendai 980-8578, Japan
naka@zisin.gp.tohoku.ac.jp

Manuscript received 25 April 2012